Master's Thesis

MULTI-MODAL REGISTRATION OF MICRO-COMPUTED TOMOGRAPHY AND MAGNETIC RESONANCE IMAGING FOR DEVELOPMENT OF THREE-DIMENSIONAL MODELS OF ARTICULAR JOINTS.

Summer Term 2006

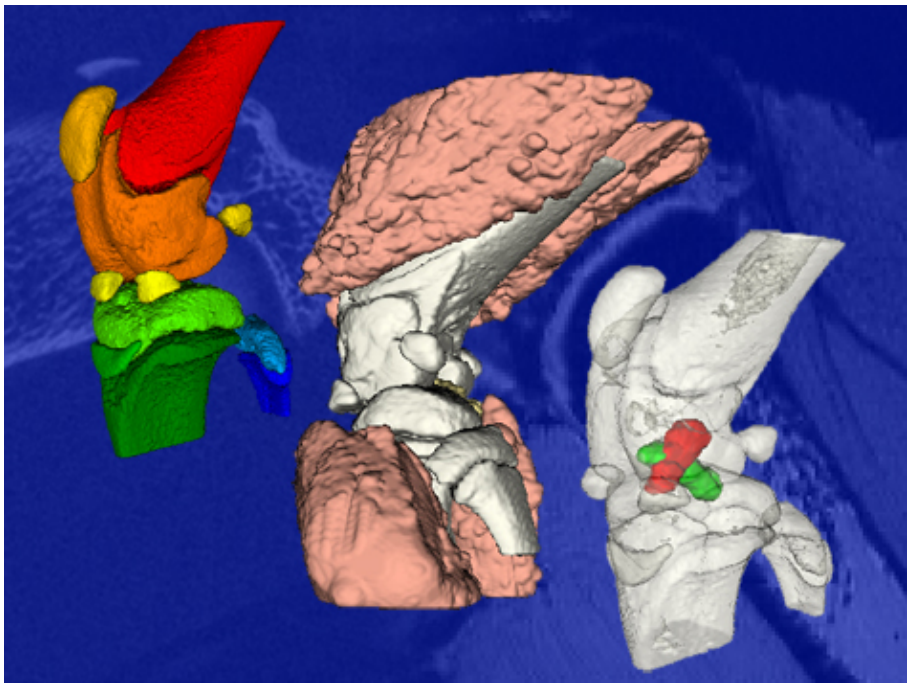

Author: Etienne Schwyter

Advisors: Dr. Steven Boyd, Prof. Dr. Ralph Müller

Calgary, September 29, 2006

MASTER'S THESIS
D-ITET, SS 2006
Etienne Schwyter

MULTI-MODAL REGISTRATION OF MICRO-COMPUTED TOMOGRAPHY AND MAGNETIC RESONANCE IMAGING FOR DEVELOPMENT OF THREE-DIMENSIONAL MODELS OF ARTICULAR JOINTS

1. INTRODUCTION

Articular joints are complex organs whose major structures include soft tissues such as ligaments, tendons, cartilage and menisci, as well as hard tissues such as bone. Subsequent to a traumatic injury such as the tearing of a ligament, all the tissues in the joint are affected due to a combined effect of inflammation and altered mechanical loading of the joint. These post-traumatic changes can lead to pathological development of the joint and eventually the development of joint diseases such as osteoarthritis. The pathogenesis of osteoarthritis is not well understood, and improved image-based mathematical models may assist in the understanding of the disease progression.

The recent development of three-dimensional (3D) imaging methodologies for measurement of tissue micro-structure has opened new possibilities for understanding tissue structure. High-resolution computed tomography (micro-CT) is a relatively new technology that plays a central role in quantifying 3D bone micro-architecture, thus allowing a non-destructive, quantitative assessment of bone. However, while micro-CT is an ideal imaging technology for bone architecture, it is less well suited for measurement of soft tissues. Magnetic resonance imaging (MRI) is best suited for measurement of soft tissues, and the development of high-strength MRI systems can now provide 3D image data sufficient to assess detailed joint structures. Combining the measurements of hard tissue by micro-CT with the measurements of soft tissue by micro-MRI can provide a complete picture of the major joint structures.

Multi-modal imaging is a term used to describe the use of more than one imaging modality; for example, micro-CT and micro-MRI. Superimposing the 3D images from each modality can be performed by finding the optimum transformation (six or more degrees of freedom) based on the correlation of the two image datasets, and is termed multi-modal image registration. There are established methods developed for multi-modal imaging, however these have traditionally been applied with image data from clinical scans involving lower resolution data. For the future development of highly detailed 3D joint models that utilize data from micro-CT and micro-MRI, it will be important to establish that the same methods used for clinical data can be applied for high-resolution multi-modal image registration. Furthermore, once the

two images are transformed into the same global coordinate system, the segmentation of each of the major joint structures will be vital such that a comprehensive 3D image model can be used for subsequent mathematical modeling.

The purpose of this project is to utilize micro-MR and micro-CT to image the same joint, and to develop an approach for combining the data from each image into a singular 3D dataset representing the joint structures. This work will provide future possibilities to generate accuracy numerical models of joints, and to follow the pathogenic changes that occur to a joint following a post-traumatic injury.

2. PROJECT TASKS

- Set up a detailed time-table for the duration of the project.
- Develop a strategy for reading and processing datasets that are generated from micro-MR and micro-CT. The main task will be reading micro-MRI data and converting it into a format where our software for processing micro-CT data can be applied.
- Measure a minimum of two articular joints (mouse knee and rat knee) with both micro-MR and micro-CT. These data will form the basis for all subsequent analysis in the project.
- Investigate issues regarding multi-modal image registration, and determine the best approach for registration of micro-CT and micro-MRI. Registration code already exists in the laboratory, but it may need to be modified for multi-modal registration.
- Define an approach for segmentation of the tissues in each imaging modality, and combine the segmented tissues into a single 3D image. Methods are available for manual segmentation; combining the two segmented images will be a challenge of the project.
- Define the parameters that will be used to evaluate the multi-modal imaging approach. Evaluate the multi-modal imaging approach with respect to the size of the joints measured. Determine if there is a resolution to structure size (i.e., rat versus mouse) dependency.
- Prepare final report including introduction, methods, results, discussion and conclusion, with an appendix containing developed source code. Provide the report in print form as well as on disk, and include the measured 3D data on the disk.

3. LITERATURE

1. Hajnal JV, Hill DLG, Hawkes DJ 2001 Medical image registration, CRC Press, New York.

2. Wachsmuth L, Engelke K (2004) High-resolution imaging of osteoarthritis using microcomputed tomography. Methods Mol Med 101:231-248

3. Wachsmuth L, Keiffer R, Juretschke HP, Raiss RX, Kimmig N, Lindhorst E (2003) In vivo contrast-enhanced micro MR-imaging of experimental osteoarthritis in the rabbit knee joint at 7.1T1. Osteoarthritis Cartilage 11:891-902

4. Sonka M, Fitzpatrick JM (2000) Handbook of medical imaging-volume 2. medical image processing and analysis. Bellingham, SPIE Press

Diplomarbeit, SS 2006

Start of Thesis:	1. April 2006
End of Thesis:	30. September 2006

Thesis Supervisor ETH:

Prof. Dr. R. Müller
Institut für Biomedizinische Technik

Thesis Advisor:

Prof. S. Boyd, Ph.D.
Department of Mechanical and Manufacturing Engineering
University of Calgary, Canada
skboyd@ucalgary.ca

Zürich, den 1. Dezember 2005

Preface

I would first like to thank everyone who supported me throughout my Master's thesis. In particular, I wish to express my appreciation to my advisor, Dr. Steven Boyd, for his support, encouragement and advice which contributed to the success of my project. Furthermore, thanks goes to Dr. John Matyas, Tadeusz Foniok, David Kirk and Peter Byrne for their expert advice and help concerning the μMRI scans and the production of the multi-modality phantom. Last but not least, a special thanks goes to my supervisor Prof. Dr. Ralph Müller, who offered the opportunity to write my Master's thesis at the University of Calgary in Canada. It has been an intensive, but very enjoyable time!

I hope that this work sets a corner-stone for future numerical analysis, for a better understanding of disease- or injury-related pathogenic changes in articular joints.

Etienne Schwyter

Abstract

Introduction: Previous studies have shown that traumatic injuries cause inflammation and altered loading of the joints. Although, not yet well understood, these pathogenic changes may lead to osteoarthritis.

The recent development of μCT and μMRI imaging methods have opened new possibilities in the evaluation of micro-structural tissue changes. High resolution computer tomography (CT) offers insight into bone architecture, whereas high field magnet resonance imaging (MRI) devices offer high resolution, information and contrast for soft tissue.

Task: Both, μCT and μMR images of an articular joint are to be acquired and methods developed for combining these datasets in a single 3D joint model. Therefore, various programs are to be implemented to register, segment and fuse multi-modality images. Finally, critical parameters in the multi-modal imaging approach are to be evaluated.

Method: The project is divided into four main steps: Acquiring data with μCT and μMRI scanners; aligning the multi-modal images with intensity- or fiducial marker-based registration methods; segmenting the various tissue types in the images into independent partitions and, finally, fusing the partitions to create one single 3D model containing information from both scanning methodologies.

To investigate the quality of the final joint model, phantom accuracy and precision measurement analysis have been performed on each processing step.

Results & Discussion: Software for the registration, segmentation and fusion of images has been developed.

The accuracy and precision results obtained are strongly dependent on the quality and resolution of the acquired images. Higher scan resolutions lead to images closer to reality, hence more accurate 3D models. However, with an increased resolution, the MR image quality (signal-to-noise ratio) decreases. This image information loss results in lower registration and segmentation accuracies. The MR image information can be optimized for samples previously soaked in contrast agent. Due to

the thin structure of cartilage, tissue can be extracted more accurately if scanned with the CT device.

Image alignment worked excellently for fiducial marker-based registrations as well as intensity-based registrations. The fiducial marker-based approach performs significantly faster and is applicable for images of arbitrary size.

The implemented graphical user interface-based segmentation program partitions bone structures, as well as soft-tissue, quickly and accurately. Its performance, however, depends strongly on the quality and resolution of the input images. Finally a simple fusion program merges the partitions together.

This report introduces an appropriate method for an accurate creation of three dimensional joint models based on μCT and μMR images. The implemented programs simplify and accelerate the processing steps and can be used in many other related imaging applications.

Outlook: In the near future numerical analysis of such three dimensional models will monitor the force displacement and force related changes induced by traumatic injuries. This may help to improve the prevention and treatments of bone and joint diseases such as osteoporosis and osteoarthritis.

Contents

1 Introduction **1**

2 Overview **3**

I Data Acquisition **5**

3 Medical Imaging an Introduction **7**
3.1 CT Scanner 8
3.2 MRI 9

4 Accuracy and Precision **13**
4.1 Introduction 13
4.2 Phantom 14
4.3 Scan Methods 17
4.3.1 CT Scanner 17
4.3.2 MRI Scanner 18
4.3.3 Laser Scanner 19
4.3.4 Thickness Measurement 21
4.4 Results 25
4.5 Discussion 29

5 Sample Scans **31**
5.1 Introduction 31
5.2 Scan Methods 32
5.2.1 MRI without Contrast Agent 32
5.2.2 MRI Scan with Contrast Agent 32
5.2.3 CT Scan without Contrast Agent 33
5.2.4 CT Scan with Contrast Agent 33
5.3 Results 34
5.4 Discussion 36

II Registration **39**

6 Introduction **41**

7 Registration Methods **43**
7.1 Intensity Based Registration 44
7.1.1 Metrics 45
7.1.2 Optimizer 46
7.1.3 Interpolator 46
7.1.4 Multi-Resolution Registration 47
7.2 Fiducial Marker-Based Registration 48
7.2.1 Fiducial Markers 48
7.2.2 Fiducial Registration 51

8 Accuracy and Precision **53**
8.1 Method 53
8.2 Results 54
8.3 Discussion 58

9 Sample Registration **61**
9.1 Method 61
9.2 Results 62
9.3 Discussion 64

III Segmentation **65**

10 Introduction **67**

11 itkSNAP **69**
11.1 Segmentation Method 69
11.1.1 Geodesic Active Contouring 70
11.1.2 Region Competition 70
11.1.3 Level-Set Method 72

12 mySNAP **73**
12.1 Denoise Filter 73
12.1.1 Discrete Gaussian Image Filter 74
12.1.2 Gradient Anisotropic Diffusion Filter 74
12.1.3 Min/Max Curvature Flow Filter 75
12.1.4 Erode&Dilate Filter 76

12.2 Edge Filter 79
12.2.1 Gradient Magnitude Filter 79
12.2.2 Zero Crossing Filter 80
12.2.3 Canny Edge Detection Filter 81
12.3 AIM compatibility 82
12.4 Logfile 82

13 Accuracy and precision **83**
13.1 Method 83
13.2 Result 85
13.3 Discussion 87

14 Sample Segmentation **89**
14.1 Method 89
14.2 Results 90
14.3 Discussion 91

IV Image Fusion **93**

15 Introduction **95**

16 Over-All Accuracy and Precision **97**

17 3D Model **99**
17.1 Method 99
17.2 Results 99
17.3 Discussion 102

Conclusion **103**

Outlook **105**

Appendix **111**

A Phantom Drawings **113**

B Data Acquisition Settings **119**
B.1 CT Scanner . . . 119
B.2 MR Scanner . . . 120
B.3 Laser Scanner . . . 121

C Thickness Measurement Settings **123**
C.1 Pre-Filter Settings . . . 123
C.2 SiteSpecificThickness Measurement Settings . . . 124

D Thickness Measurement Results **125**
D.1 Phantom Laser Scan . . . 125
D.2 Phantom CT Scan . . . 125
D.3 Phantom MRI Scan . . . 126
D.4 Acquisition Accuracy and Precision Results . . . 126

E Registration Results **127**
E.1 Fiducial Marker-Based Registration . . . 127
E.2 Intensity-Based Registration . . . 128
E.3 Intensity-Based Registration with Offset Variation . . . 128
E.4 Intra-Modality Registration Results . . . 129

F Segmentation Results **131**
F.1 Segmentation Accuracy and Precision Results . . . 131
F.2 Segmentation Results with Decreasing CNR . . . 132
F.3 Segmentation Results with Increasing Number of Seed Points . . . 133
F.4 Segmentation Results with Changing Segmentation Parameters . . . 133

G Segmented Rat Knee Joint **135**

H Libraries and Programming Languages **137**
H.1 Visualization Toolkit (VTK) . . . 137
H.2 Insight Toolkit (ITK) . . . 137
H.3 Fast Light Toolkit (FLTK) . . . 137
H.4 CMake . . . 138
H.5 Microsoft Visual C++ . . . 138

I Applications and Classes **139**
I.1 Implemented . . . 139
I.1.1 DrillingHoleRawDataFilter . . . 139
I.1.2 TrenchRawDataFilter . . . 139
I.1.3 DrillingHoleCircleFitting . . . 140
I.1.4 TrenchLineFitting . . . 140
I.1.5 AppAIMDenoiseFilter . . . 140
I.1.6 itkSimilarityRegistration . . . 141
I.1.7 itkSimilarityRegistrationFloatingPoint . . . 143
I.1.8 AppFiducialMarkerBasedRegistration . . . 143
I.1.9 vtkIntensityWeightedCentroid . . . 144
I.1.10 vtkPointBasedRegistration . . . 144
I.1.11 vtkBrukerReader . . . 145
I.1.12 AppCheckerBoard . . . 146
I.1.13 AppAIMCube . . . 147
I.1.14 AppAIMMerge . . . 147
I.1.15 AppAIMNoiseFilter . . . 148
I.1.16 AppAIMPos . . . 149
I.1.17 AppAIMRelabel . . . 149
I.1.18 mySNAP . . . 149
I.2 Used . . . 153
I.2.1 Alibre Design . . . 153
I.2.2 CUTOUT . . . 153
I.2.3 IPL . . . 153
I.2.4 SAP . . . 153
I.2.5 VIS and SHAPE . . . 153
I.2.6 SiteSpecificThickness . . . 154

Chapter 1

Introduction

Osteoarthritis is the most prevalent chronic disease. Affecting more than 50% of the population aged 65 or above [10], causing pain, functional deficits, and substantially reducing quality of life. With the aged population continually growing, the number of people suffering from the effects of osteoarthritis will considerably increase over the coming decades.

Previous studies have shown that traumatic injuries cause inflammation and altered loading of the joints. Although these mechanisms are not yet fully understood, it is thought these pathogenic changes may lead to osteoarthritis.

Recently developed three dimensional (3D) imaging methods have opened new possibilities in the evaluation of micro-structural tissue changes. High resolution computer tomography (CT) offers insight into bone architecture, whereas newly developed high field magnetic resonance imaging (MRI) devices provide high resolution images with good soft-tissue contrasts.

The combination of these two methods may increase image information content and lead to increased understanding of the complex structure of articular joints.

In the near future, numerical analysis of such three dimensional models will monitor the force displacement and force-related changes induced by traumatic injuries. This may help to optimize prevention and treatment of bone and joint diseases like osteoporosis and osteoarthritis.

Chapter 2

Overview

The creation of a 3D joint model is based on four major processing steps.

Initially, MR and CT image data has to be acquired and the images aligned (registered) for the subsequent processing steps. A segmentation program extracts bone structures from the CT image and soft-tissue from the MR dataset. The segmented partitions of both modalities are fused and form the final 3D model. The concept is illustrated in the flow-chart below (figure 2.1).

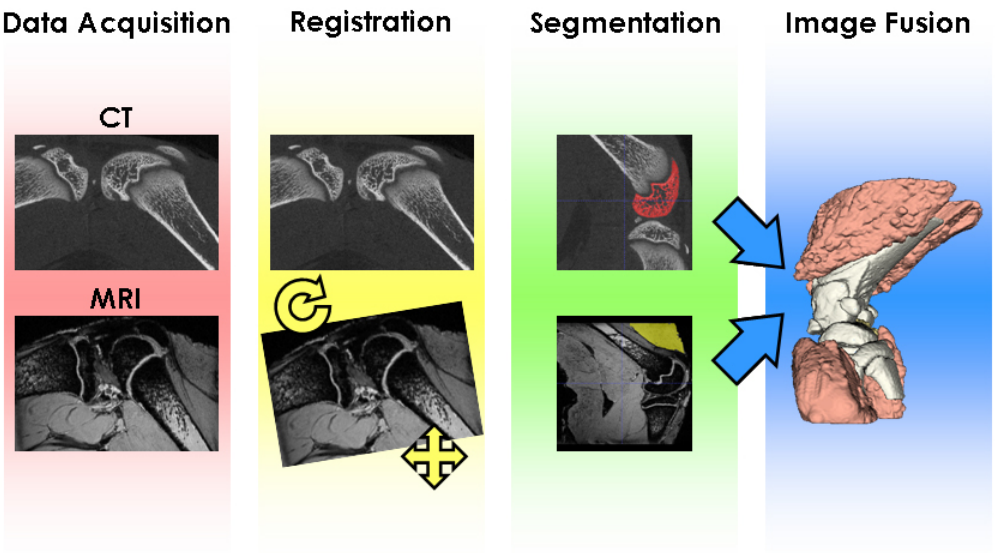

Figure 2.1: Flow-chart with the four major processing steps involved in the creation of a 3D (joint) model.

This report is divided into four main sections, each describing a separate processing step. Methods, results and discussion are presented individually for each part. Furthermore, each part contains an accuracy and precision analysis of the particular processing step.

The Appendix, lists and describes all the implemented programs. The image datasets, final 3D model and complete source code for the programs implemented, can be found on the enclosed DVD.

Part I

Data Acquisition

Chapter 3

Medical Imaging an Introduction

Over the last two decades 3D medical images have gained increasing importance in clinical applications as well as medical research. The ability to visualize and analyze tissue in three dimensions, can lead to a better understanding of various medical phenomena and increased accuracy and reliability for diagnosis.

In osteoporosis and osteoarthritis research, the invention of the CT scanner opened the door for many new research areas, as it allows bone changes to be monitored over time as well as analyzed and visualized in a 3D model.

A similar steep increase in interest could be observed for Magnet Resonance Imaging (MRI). The excellent soft-tissue contrast and non-destructive acquisition methods have made the MR scanner one of the most dominant medical imaging devices on the market.

For the development of three dimensional models of the knee joint, both CT and MRI are the imaging methods of choice. CT returns excellent images of bone structure, where as MRI is capable of visualizing soft-tissues such as muscles, tendons, ligaments or cartilage.

In subchapter 3.1 and 3.2, the functionality of both CT and MR scanners used in this study are briefly described.

3.1 CT Scanner

Since its introduction in 1972, CT technology and capabilities have been significantly improved, and CT use in clinical applications is rapidly increasing.

Fast, three dimensional and highly accurate images make CT the number one choice for research in any kind of bone diseases, like osteoporosis or osteoarthritis.

In 1917, Radon claimed that a three dimensional image of an object could be produced if one had an infinite number of projections through the object. The technology of the CT scanner is based on such two dimensional X-ray projections and their three dimensional reconstruction.

The emitted X-rays with intensity I_0 are partially absorbed dependent on the attenuation properties μ of the scanned tissue and tissue thickness t

$$I_t = I_0 \cdot e^{-\mu t} \tag{3.1}$$

The transmitted X-rays with intensity I_t are captured by a scintillator attached to a two dimensional charged coupled devices (CCD) array. A scintillator emits visible light when it is struck by X-rays, and a CCD unit transforms the light waves into an electrical charge.

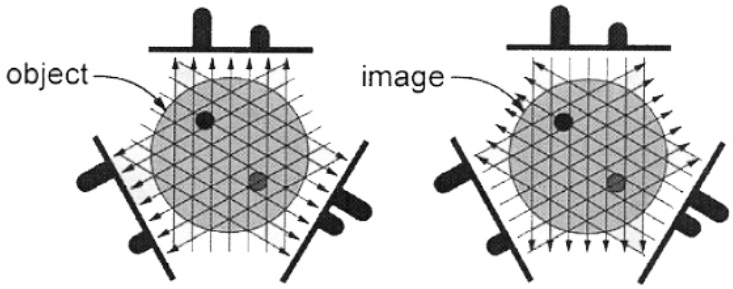

Figure 3.1: Principle of the filtered back-projection reconstruction method

X-ray emitter and detector are attached together and take multiple projections of the object from multiple angles, a three dimensional image can be reconstructed using one of many developed reconstruction algorithms. The most commonly used approach is a filtered back-projection reconstruction (figure 3.1), which essentially reverses the acquisition step by smearing the attenuation coefficient μ along the known projection line. The value μ for each projection line is evaluated by solving equation 3.1

$$\mu = ln(I_0/I_t)/t \tag{3.2}$$

Integrating the values of μ for each back-projection results in the final three dimensional CT image.

For this study, a vivaCT 40 scanner (figure 3.2) from Scanco Medical AG, Switzerland [39] was used. Its high resolution, with voxel sizes as low as 10μm, and its excellent image qualities were ideal for the creation of a 3D multi-modality knee joint model.

Figure 3.2: vivaCT 40 scanner (Scanco Medical AG, Switzerland)

3.2 MRI

MRI is an imaging method based on nuclear magnetic resonance (NMR) theory. The first scanners were clinically used in the early 1980s and not even the most optimistic of guesses would have expected that this highly complex method would come to dominate the medical imaging market within two decades.

In principle, a spinning proton can be represented with a dipole magnetic field B (figure 3.3 , left). Under the influence of an external static magnetic field B_0, the protons start to align themselves parallel or anti-parallel to B_0 (figure 3.3 , right). The magnetic field B of the protons can now be excited by an angle θ, if a radio frequency (RF) energy of specific frequency f_{RF} is applied for a specific time t.

$$\theta = f_{RF} \cdot 2\pi \cdot t \tag{3.3}$$

However, if the RF energy is not applied at a frequency corresponding to the Larmor frequency f_L, the resultant magnetic field B_{RF} will not be stationary in the

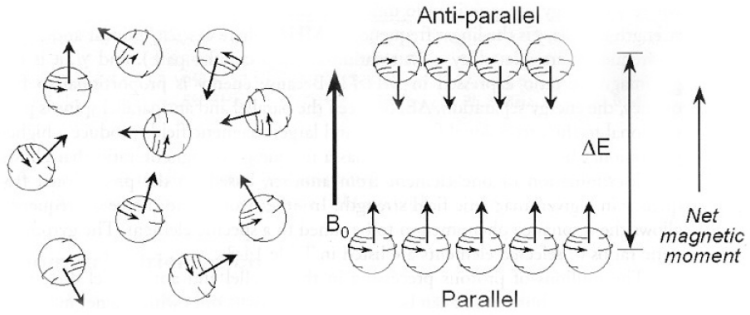

Figure 3.3: Simplified distribution of "free" protons with and without an external magnetic field B_0

rotating frame and the resonance between the two magnetic fields does not occur.

Excited atoms (mostly H-atoms) produce a signal with amplitude dependent on relaxation characteristics and spin density (see figure 3.4). This signal is detected by a receiver antenna.

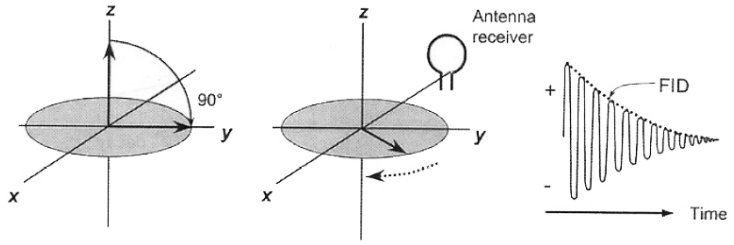

Figure 3.4: A) Flipped spin (magnetization) by a 90 degrees RF pulse; B) Precessing of the magnetization with f_L; C) Received antenna signal with decreasing amplitude due to the dephasing process

In order to distinguish one voxel in space from another, non-uniformities in the magnetic field are introduced with the use of gradient coils. These coils produce small magnetic field gradients in the x, y and z direction that can be used to determine spatial information. The small change in magnetic field strength will have a corresponding small change in Larmor frequency as given by

$$f_L(x, y, z) = \frac{\gamma}{2\pi} \cdot (B_0 + G_x(x) + G_y(y) + G_z(z)) \tag{3.4}$$

The gyro magnetic ratio γ is unique for each element and determined by G_x, G_y and G_z which are the position-dependent magnetic fields added to the static magnetic field B_0 (see figure 3.5).

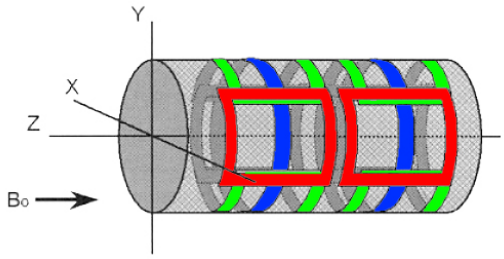

Figure 3.5: Field gradients are produced by three separate coils (red, green, blue) placed within the core of the magnet.

Magnet resonance imaging's vital use in today's medical research, is due to its ability to manipulate and adjust tissue contrast by choosing different gradient and pulse sequences.

In this study, a high resolution 9.4T μMRI device from Varian Inc., USA [44] was used to extract different soft tissues such as muscles, tendons, ligaments and cartilage. With a minimum voxel size of approximately 50μm, this device has a resolution 20 times higher than its clinical (1.5T) counterparts.

Figure 3.6: 9.4T 21cm bore MRI scanner from Varian Inc., USA

The voxel size is, in general, defined by two parameters: the radio frequency bandwidth and the gradient field strengths. Figure 3.7 shows that with narrower band width and a higher gradient strength, smaller slice thicknesses and hence,

smaller voxel sizes, can be achieved. However, due to physical limitations, chemical shift artifacts and other undesired image characteristics, the trade-off between image quality and image resolution must be considered when determining RF bandwidth and gradient field strength.

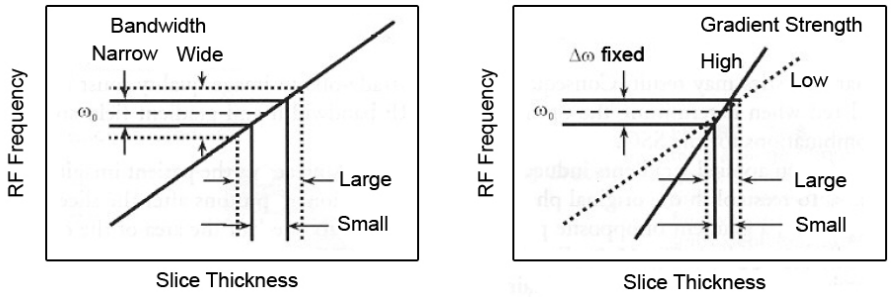

Figure 3.7: Dependency of slice thickness on the RF bandwidth and gradient field strength.

For smaller voxel sizes, the static magnetic field B_0 has to be increased simultaneously to receive sufficient signal from a significantly smaller area.

Chapter 4

Accuracy and Precision

4.1 Introduction

The term accuracy is used to describe the difference between a measured value and the real value. Precision is the degree to which a series of measurements differ from one another. Figure 4.1, illustrates the difference, with accuracy represented as the distance from the center and precision as the repeatability of the measurements. Both values are independent from each other, and a measurement can be accurate, precise, both or neither.

Figure 4.1: Accuracy and precision illustrated on a target. Left: High accuracy, but low precision. Right: High precision, but low accuracy.

In a more mathematical way, accuracy can be described as the distance between the measurements mean and reference value, whereas precision is related to the standard deviation of the measurements, as illustrated in figure 4.2.

In the medical imaging field, both values are of major importance. The acquired data must be accurate to obtain images which resemble the real sample, and they must also be precise to be able to make comparative studies over time. The second

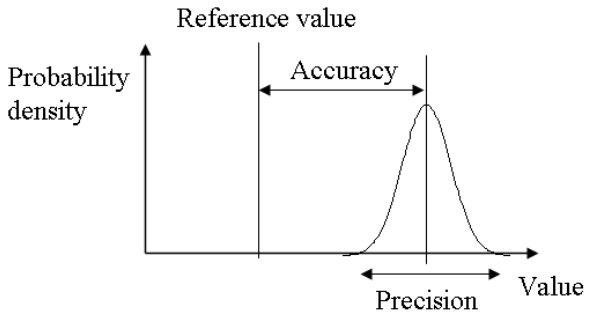

Figure 4.2: Mathematical interpretation of accuracy and precision.

property can be considered more critical as in most cases multiple scans are necessary to obtain significant results.

In this study, the accuracy and precision of the CT and MRI scanners have been evaluated. These values form the cornerstones for all subsequent processing steps. Registration as well as segmentation further decrease accuracy and precision values of the images. The methods and results of these measurements will be discussed in more detail in subchapters 4.4 and 4.5.

4.2 Phantom

The creation of a three dimensional knee joint model and subsequent finite element (FE) analysis may lead to a proper understanding of the pathogenesis of osteoarthritis.

A 3D model only reproduces valid data if the model is actually representative of reality i.e. the model must be an accurate reproduction of the real knee joint. Accuracy and precision are therefore the most important values when building a model. Previous studies [11, 30] have shown that these values are best evaluated using a phantom.

The main advantages of a 3D phantom are depicted below:

- **Rigidity:** A phantom is fabricated out of solids and therefore does not change its shape during or between the scans. This is probably the main and most critical factor concerning accuracy and precision measurements with phantoms.
- **Simplicity:** A phantom is usually less complicated in design than a real tissue sample. This simplifies the subsequent analysis significantly.

- **Regularity:** The thickness deviations or volume errors when imaging phantoms are usually in orders of magnitude smaller than in reality.
- **Visibility:** If desired, the contrast between two different objects can be enhanced by choosing different phantom materials or contrast agent concentrations.
- **Durability:** The phantom can be used repeatedly without any deterioration of the material.

Unfortunately, such phantoms are not commonly available and a consolidated standard does not exist. A three dimensional phantom was specifically designed and fabricated for the purpose of this study. In opposition to other phantom related works [7, 34], the materials used had to be both CT and MR compatible. This rules out several, in general more simple, approaches.

The phantom mainly consists of 4 polymethylmethacrylate (PMMA) pieces. PMMA is a solid and transparent material which has minimal X-ray absorption and returns no MR signal. The major component, called phantom cylinder, consists of a 9.5mm thick rod with well-defined and positioned trenches and drilling holes. The trenches with perpendicular side walls have a uniform thickness of 3.2mm and lie in the XY, XZ respectively YZ plane. Three additional trenches, rotated by 45 degrees around the X, Y or Z axis have also been placed. For tilted planes, the accuracy might be reduced, as the edge voxels will be an interpolation of two different intensities. This is especially important for non-isotropic voxels (see figure 4.3).

Figure 4.3: A) Image of a 45 degrees phantom trench. B) Scan with isotropic voxel size. C) Scan with non-isotropic voxel size.

To investigate the accuracy and precision of smaller structures, a set of holes with different diameters have been drilled along each axis, and at 45 degrees, equal to the orientations of the trenches. Using diameters of 2.4, 1.2 and 0.6mm the drilling holes are approximately one order of magnitude larger then the voxel size.

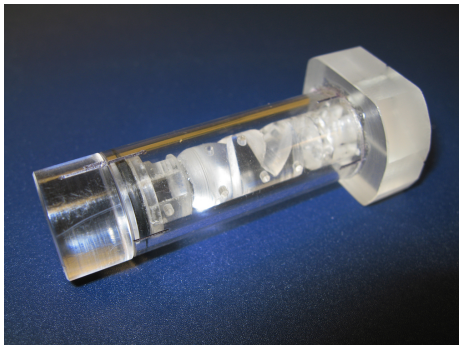

Figure 4.4: Picture of MRI and CT compatible accuracy and precision phantom.

The phantom cylinder (see figure 4.4) is attached to the front seal. The PMMA tube, which encloses the phantom cylinder, is glued to the back seal. An O-ring provides a tight seal between the two separate phantom components, allowing for rotation of the phantom cylinder throughout 360 degrees (i.e. around the z-axis). The angles 0, 2, 4 and 6 degrees are marked on the surface of the front seal. The back seal has four grounded flats tilting the phantom by 0, 2, 4 or 6 degrees around the y-axis. These extra features provide for more options in evaluating the accuracy and precision of MR and CT scanners.

The phantom can be filled with any CT- and MRI-compatible liquid. Therefore, the contrast and intensity can be optimized for each individual measurement. This is especially useful for image registration processes, where the intensity and contrast values should be set as close as possible to real tissue values. For this study, a water/iodine solution, in a 1:20 ratio was found to be ideal.

Filling the phantom was critical and had to be handled with great care. The two phantom pieces were placed separately into a container filled with the water/iodine solution. The solution was then degassed in a vacuum chamber for 4 hours, to eliminate any trapped air bubbles in the liquid filled phantom. Air/water interfaces introduce significant MR artifacts and must be appropriately removed.

As water is hardly compressible, a simple and effective system was designed to release the overpressure in the phantom chamber, allowing for the two phantom parts to be tightly sealed.

The pressure release system consists of two screw holes in the back seal of the phantom (see figure 4.5 left). One of the screws (A) has to be taken out while the other one (B) is screwed in completely. Thus, the overpressure can escape trough drilling hole A while the two phantom parts are pressed together underneath the solution surface (see figure 4.5 middle). In a second step, screw A is screwed in, while

screw B is simultaneously released, leveling the pressure in the phantom chamber (see figure 4.5 right). If both screws are half-way in, the phantom is filled and tightly sealed without any trapped air.
Schematics and pictures of the 3D phantom model are attached in Appendix A.

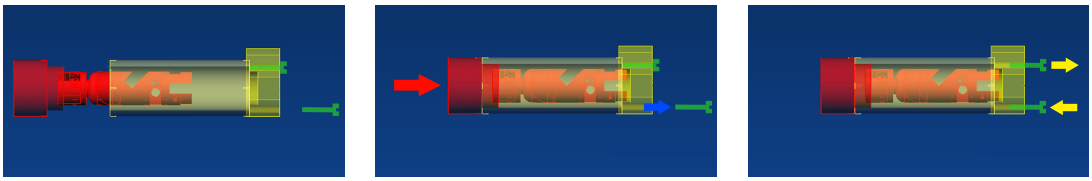

Figure 4.5: Phantom sealing procedure, from left to right.

4.3 Scan Methods

4.3.1 CT Scanner

To determine accuracy and precision, repeated measurements of the same well-defined sample need to be taken and compared. An MRI- and CT- compatible phantom was designed and manufactured for this purpose (previously described in subchapter 4.2).

The phantom was scanned 3 times. Prior to each data acquisition, the sample was rotated 90 degrees, to take scanner-specific inhomogeneities into account. In each 3D data set, a drilling hole and trench was separately cut out and pre-filtered. The filtering step was necessary, since the accuracy and precision measurements were based on a thickness measurement, evaluated with Mattmann and Kuhn's [27] SiteSpecificThickness program. In a nut shell, this program determines the shortest distance for each point on a thresholded iso-surface, based on iso-surface normals and a growing sphere. A detailed description will follow in subchapter 4.3.4.1 and Appendix I.2.6.

Small iso-surface bubbles occurred in the thresholded image (see figure 4.6) due to acquisition induced noise. These artifacts made a reliable thickness measurement impossible, since the shortest sphere diameter is no more the distance between the trench plains, but the distance between the trench wall and the artifact. Therefore, pre-filtering was required.

However, filtering is a direct change of the image data and thus might lead to information loss. This deficit could be minimized by using the opening and closing denoise filter originally developed by Matheron and Serra [42] (further described in subchapter 12.1.4).

Figure 4.6: Left: Slice view of a CT scanned and thresholded drilling hole. Right: Same drilling hole, but previously erode&dilate filtered.

To keep the induced error low, the parameters for the pre-filter as well as the thickness measurement were maintained for all scans. Table C.1 and C.2 in Appendix C list all parameters.

4.3.2 MRI Scanner

In principle, the accuracy and precision measurement method for MRI is identical to the method used for the CT scans.

One small change was required, to compensate for the differences between the two data acquisition methods. The threshold level for the iso-surface used in the SiteSpecificThickness program, was adjusted due to enhanced intensity signals in the MRI scan. The adjustment was based on a visual control (see figure 4.7).

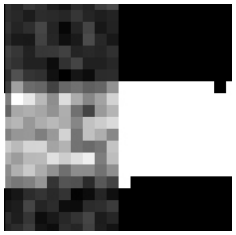

Figure 4.7: Left: Original MR image slice through a phantom drilling hole. Right: Adjusted threshold to match the edges as good as possible.

4.3.3 Laser Scanner

The accuracy of a series of measurements can only be determined if a reference value, also called ground truth, exists. Obviously, this method has to have a higher resolution than that of the CT and MRI devices.

The SLS 2000 laser scanner from LMI Selcom Inc. [22] has a maximum resolution in the sub-μm range, making it most suitable for determining the "real" thickness of the drilling holes and trenches. The near-infrared semi conductor laser diode illuminates a spot on the surface of the object to be measured. The detector is situated at the back of the receiver, similar to the retina of the human eye. Depending on the distance between the laser scanner and the sample, the laser beam will hit a different location on the detector. The detector is a high resolution, light sensitive unit, which converts the light into an electrical signal which can be used to calculate the actual distance of the object (see figure 4.8).

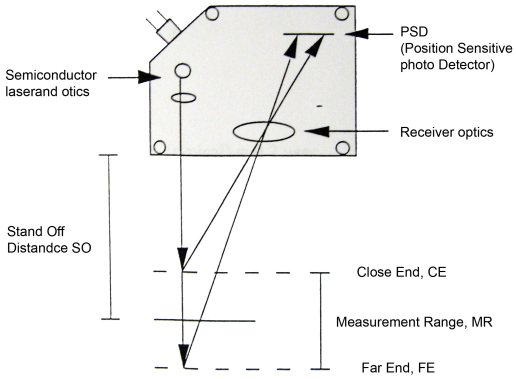

Figure 4.8: Functionality of the SLS 2000 laser scanner.

With 16'000 measurement sequences per second, this method is relatively fast and highly accurate. The error is typically less than 0.2%.

Major difficulties appeared due to the high transparency of the phantom. Semi-transparent material scatters enough light to produce a stable measurement, but there is also a significant contribution of light from internal and background reflections. The result is a position reading that is below the actual surface. Due to this drawback a 3D profile laser scan of the sample was not possible.

Nevertheless, the drilling hole and trench thicknesses could be determined, since the laser signal peeked in the edge areas of the phantom. The distance between the peeks represents the thickness of the geometric structures.

This measurement method is independent of the absolute distance between the

scanner and the sample. It only depends on the relative signal changes in the edge areas, as the trench and drilling hole thickness is measured in the transverse and not in longitudinal direction.

To sharpen the peak signal, and therefore increasing accuracy of the measurement, a black, laser light absorbing hard paper was placed underneath the phantom to reduce unwanted light reflections. The side walls were aligned absolutely parallel to the laser beam to avoid thickness underestimation. Based on simple projection geometry, the edges move closer together if the phantom is tilted (see figure 4.9). The alignment was optimized until the rising slope in the laser signal (marked in red) vanished.

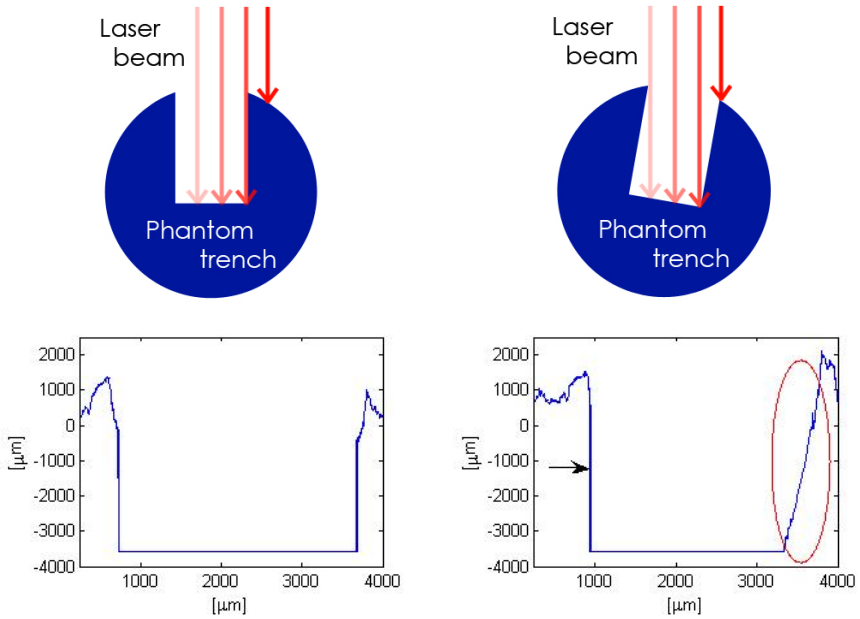

Figure 4.9: Left: Parallel alignment of trench side walls with laser beam. Right: Tilted phantom. Thus, the edges of the trench move closer together which results in an underestimation of the trench thickness. Beneath the images, the corresponding laser signal is depicted.

The same trench and drilling holes scanned previously with the MRI and CT devices were laser scanned for three times. For each measurement, the laser scanner was recalibrated and the phantom repositioned. The settings are listed in table B.

4.3.4 Thickness Measurement

4.3.4.1 CT and MRI

After CT and MRI scans of the phantom, the trenches and drilling holes were extracted for the subsequent thickness measurements.

In general, all the trench and drilling hole triplets have the same geometric properties, but fabrication-induced mean thickness variations of approximately 50μm might effect the reliability of the accuracy and precision measurements. Thus, the thickness measurements for all the scans were taken in the same region of one phantom trench respectively drilling hole. The measurement regions are marked in the picture below (4.10).

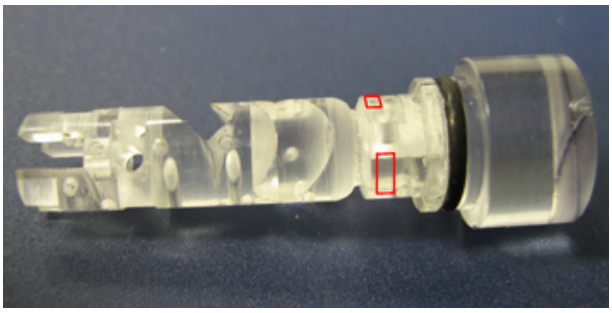

Figure 4.10: Scan area for trench and drilling hole thickness measurement.

For the thickness measurement of the CT and MRI data, SiteSpecificThickness, a surface-based approach implemented by Mattmann and Kuhn [27],was used. The basic idea is to increase the diameter of a sphere inside an object, until the sphere intersects with the object's surface (depicted in figure 4.11).

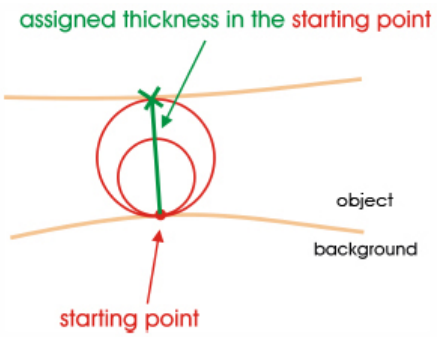

Figure 4.11: Basic idea behind the sphere growing method.

The center of the sphere lies on the negative normal of the object surface. However, if the surface is concave or roughened, the sphere may intersect first with a point close to the starting point (see figure 4.12 left). To avoid this problem, the angle between the two normals is calculated using the dot-product, and intersections with normal angles below ±60 degrees are discarded. If the orientation is deemed incorrect, the algorithm continues searching for the next intersecting point.

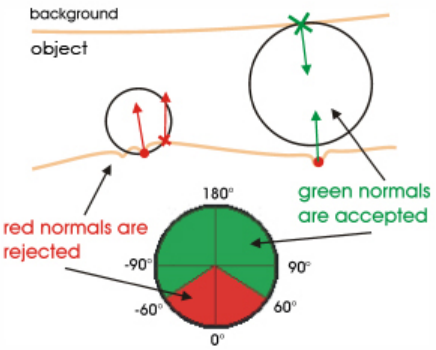

Figure 4.12: Sphere growing with additional orientation checking.

For extremely rough surfaces, the angle approach is not sufficient, as the angles of the normal might easily exceed ±60 degrees. Therefore a variable offset was added to inhibit these intersections (see figure 4.13).

Provided there is no intersection, the sphere radius is increased. If an intersection with "wrong" normal orientation is found, the offset is increased to evade such crossovers.

This process is repeated for all marching cube surface points until mean thickness and standard deviation for the whole object are calculated.

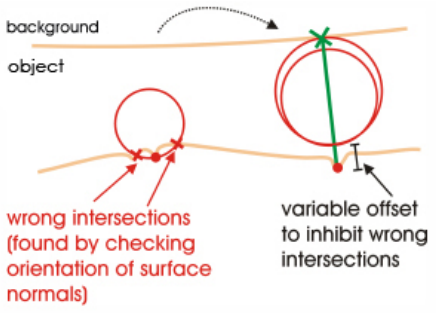

Figure 4.13: Sphere growing in the inversed normal direction with an additional offset.

For more detail on the usage of this program see Appendix I.2.6.

4.3.4.2 Laser

As mentioned earlier, the ground truth thickness was evaluated by laser scan. The signal peaked in edge points. Thus, the edges could easily be reconstructed from the raw data by extracting the points with the highest and lowest intensity values respectively. This data preprocessing step was computed using Matlab [26] functions "TrenchRawDataFilter.m" and "DrillingHoleRawDataFilter.m" further described in Appendix I.1.2 and I.1.1.

In a second step, the functions "TrenchLineFitting.m" and "DrillingHoleCircleFitting.m" (see Appendix I.1.4 and I.1.3) fit two lines or a circle respectively to the filtered edge points.

Both functions are based on a least squares approach and are described separately in the next two sections.

Circle Fitting

For the circle fitting, the Gauss-Newton method [13] was used to solve the non-linear least squares problem. Then the non-linear least square problem can be defined as

$$\sum_{i=1}^{m} f_i(u)^2 = min \tag{4.1}$$

$u = [u_1, \ldots, u_n]^T$ is a vector of unknowns and the nonlinear system of m equations $f(u)$ is considered zero. The solution of equation 4.1 is approximated by $u + h$. Developing

$$f(u) = [f_1(u), f_2(u), \ldots, f_m(u)]^T \tag{4.2}$$

around u in a Taylor series [13],

$$f(u + h) = f(u) + \Im(u) \cdot h = 0 \tag{4.3}$$

is obtained, where $\Im$ is the Jacobian matrix. Equation 4.3 now can be solved for the correction vector h as a linear least squares problem.

$$\Im(u) \cdot h = -f(u) \tag{4.4}$$

The consequent Gauss-Newton iteration method consists of two steps:

1. Solving equation 4.3 for h
2. Updating the approximation of the unknowns $u = u + h$

In the case of a circle, the distance d_i between the measurement points x_i and the points on the circumference of the circle has to be minimized.

$$d_i^2 = (\|z - x_i\| - r)^2 \tag{4.5}$$

Hence, the nonlinear least squares problem is given by

$$\sum_{i=1}^{m} d_i(u)^2 = min \tag{4.6}$$

where $u = [z_1, z_2, r]^T$ is the unknown position and radius. Equation 4.7 shows the Jacobian matrix which is defined as the partial derivatives $\partial d_i(u)/\partial u_j$.

$$\Im(u) = \begin{bmatrix} \frac{u_1 - x_{11}}{\sqrt{(u_1 - x_{11})^2 + (u_2 - x_{12})^2}} & \frac{u_2 - x_{12}}{\sqrt{(u_1 - x_{11})^2 + (u_2 - x_{12})^2}} & -1 \\ \vdots & \vdots & \vdots \\ \frac{u_1 - x_{m1}}{\sqrt{(u_1 - x_{m1})^2 + (u_2 - x_{m2})^2}} & \frac{u_2 - x_{m2}}{\sqrt{(u_1 - x_{m1})^2 + (u_2 - x_{m2})^2}} & -1 \end{bmatrix} \tag{4.7}$$

The Gauss-Newton iterator starts with a user defined initial guess of the centroid z and the radius r, and returns the best fit after the method converged.

Line Fitting

Similar to circle fitting, the linear fitting is based on minimizing the squares of the distances between the line and the measurement points (x_i, y_i).

$$d_i^2 = (y_i - (a + b \cdot x_i))^2 \tag{4.8}$$

where a defines the offset and b the slope of the fitted line. In this case, equation 4.6 is set to zero and the Jacobian matrix calculated.

$$\Im(a, b) = \begin{bmatrix} -2 \cdot (y_1 - (a + b \cdot x_1)) & -2 \cdot (y_1 - (a + b \cdot x_1)) \cdot x_1 \\ \vdots & \vdots \\ -2 \cdot (y_m - (a + b \cdot x_m)) & -2 \cdot (y_m - (a + b \cdot x_m)) \cdot x_m \end{bmatrix} \tag{4.9}$$

Unlike the circle fitting approach, unknowns a and b can be separated,

$$\begin{bmatrix} m & \sum_{i=1}^{m} x_i \\ \sum_{i=1}^{m} x_i & \sum_{i=1}^{m} x_i^2 \end{bmatrix} \begin{bmatrix} a \\ b \end{bmatrix} = \begin{bmatrix} \sum_{i=1}^{m} y_i \\ \sum_{i=1}^{m} x_i y_i \end{bmatrix} \tag{4.10}$$

and finally solved (for a and b) without using the Gauss-Newton approach.

$$a = \bar{y} - b \cdot \bar{x} = \frac{\bar{y}(\sum_{i=1}^{m} x_i^2) - \bar{x}(\sum_{i=1}^{m} x_i y_i)}{\sum_{i=1}^{m} x_i^2 - m\bar{x}^2} \tag{4.11}$$

$$b = \frac{\sum_{i=1}^{m} x_i y_i - n\bar{x}\bar{y}}{\sum_{i=1}^{m} x_i^2 - m\bar{x}^2} \tag{4.12}$$

This algorithm is applied to both sets of edge points in the filtered raw data. The mean distance between the two fitted lines is calculated and corrected by the angle difference between the two lines. For angles other then zero, the thickness would be overestimated (see figure 4.14).

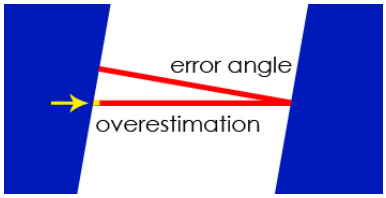

Figure 4.14: Top view on scan area. The thickness t has to be corrected by error angle α.

4.4 Results

The laser thickness measurement results form the basis of the accuracy and precision evaluations of the CT and MRI devices.

The laser-based ground truth results are illustrated in table D.1. The average drilling hole and trench thickness is 661.9±4.2μm and 3270.3±4.8μm respectively.

Figures 4.15 and 4.16 show the circle and line best fits evaluated with the implemented Matlab functions.

Due to the presence of noise in the images, small iso-surface bubbles occurred in the thresholded image (figure 4.6, left). The opening and closing filter successfully removed all the artifact while preserving the target structure (figure 4.6, right).

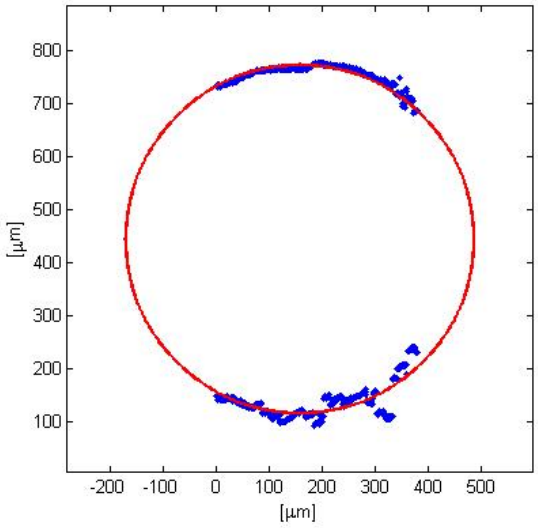

Figure 4.15: Circle best fit for the laser scanned drilling hole dataset.

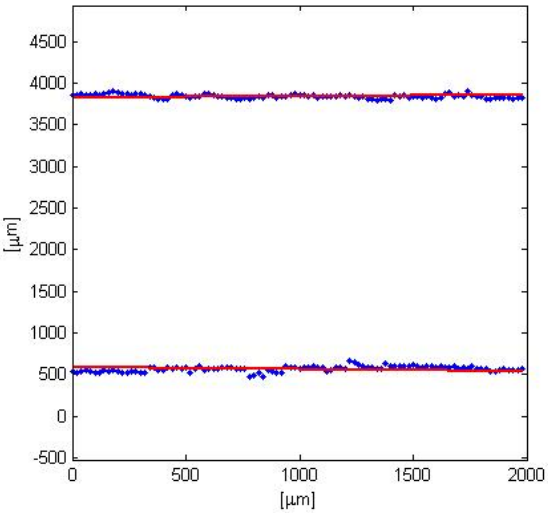

Figure 4.16: Line best fit for the laser scanned trench dataset.

The SiteSpecificThickness program determines the median thickness m and standard deviation d for all iso-surface points N. Tables D.2 and D.3 as well as figures 4.17 and 4.18 show all CT and MRI measurement results, with final accuracy and precision values of the scanners listed in table D.4.

Figures 4.19 and 4.20 depict a colored iso-surface of the drilling hole and trench. Blue color indicates low thicknesses, and red indicates high thicknesses.

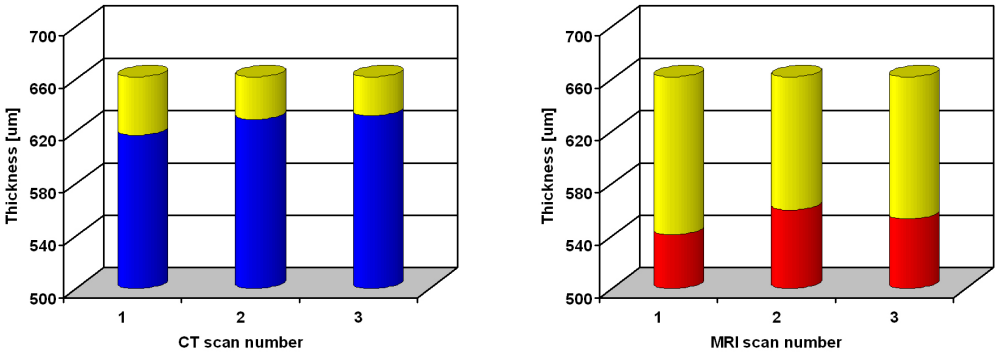

Figure 4.17: Graph with thickness measurement results of the drilling hole. CT (blue), MRI (red), are compared with the mean thickness evaluated with the laser scanner (yellow).

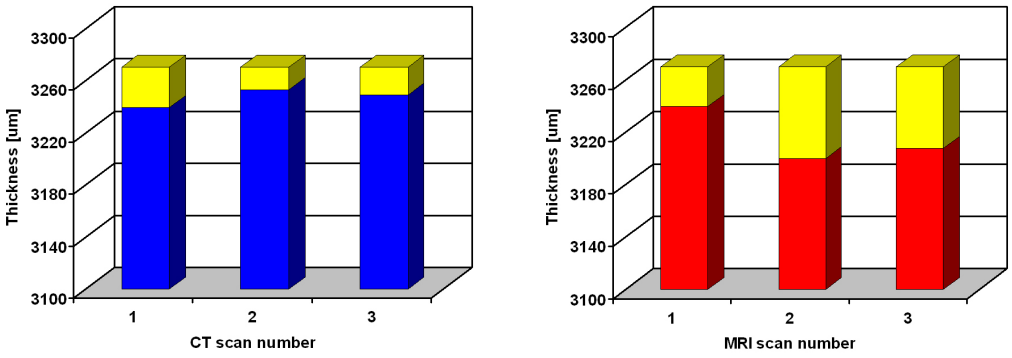

Figure 4.18: Graph with thickness measurement results of the trench. CT (blue), MRI (red), are compared with the mean thickness evaluated with the laser scanner (yellow).

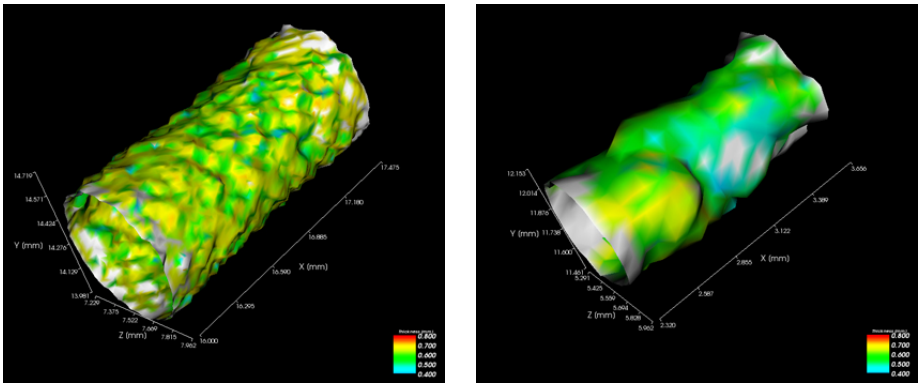

Figure 4.19: SiteSpecificThickness measurement results of the drilling hole.

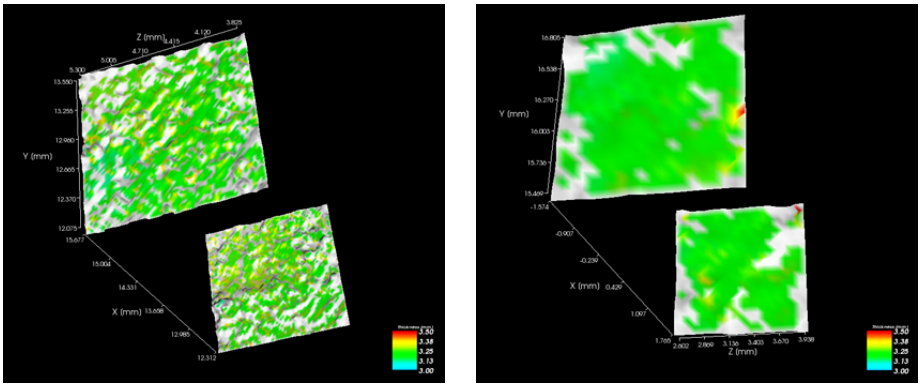

Figure 4.20: SiteSpecificThickness measurement results of the trench.

4.5 Discussion

The thickness standard deviation of the laser-scanned samples is 4.2μm and 4.8μm respectively and is significantly lower then for CT and MRI. The laser scanner manufacturer furthermore claims that the measurement error lies beneath 0.2% of the scan range. Therefore, the maximum offset for both, the drilling hole and the trench, should be in the range of 2μm and 8μm respectively.

Note that the precision values are calculated from the mean thickness values of the individual scans. The standard deviation of the individual scans is higher due to the rough surface caused by the drills and saw blades used for the phantom fabrication (see tables D.2 and D.3).

The high precision and assumed high accuracy of the laser scanner, justifies the use of these results as a "gold standard".

The mean thickness values of the CT scans are stunningly close to the measured ground truth. The accuracy is in the order of a single voxel size (21μm). This result is concordant the partial volume effect theorem, which circumstantiates that the absolute thickness error in an image will be at least one voxel [23].
The extremely small variation of the mean thickness values (7.9μm and 7.2μm respectively) show that repetitive studies might lead to highly reliable results.

Nevertheless, the accuracy drops by over 50%, when measuring small structures (such as drilling holes) instead of large structures (trench). A decrease in thickness results in a diminished number of voxels in the volume of interest and the partial volume effect has a more significant influence on the result.

Similar to the CT scans, the MR images are fairly accurate, with an average offset from the ground truth of only 54.3μm for the trench. The standard deviation of the individual scans is again in the range of a single voxel size. Since the voxel size is approximately three times larger than with CT, the standard deviation similarly increases.

For the MR scanner with a voxel size of 70μm, only eight consecutive voxels fit within the drilling hole. Therefore, the accuracy drops by 100% due to the major influence of the partial volume effect.

The standard deviation, on the other hand, is unexpectedly low. A value far above the measured 21.2μm would be expected. The three measurements may just coincidently lie close together. With an increased number of scans, the standard deviation might level out with the variation obtained in the trench thickness measurements.

Due to air bubbles trapped in the phantom, heavy air/water interface distortions occurred in the MR images (see figure 4.21). Thus, the phantom degas time should be increased to at least 24 hours, in order to avoid image quality reductions.

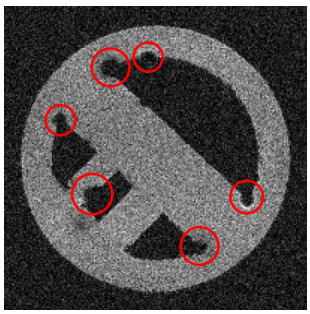

Figure 4.21: Trapped air bubbles in the phantom lead to severe distortions in the MR images.

As shown in figure 4.19 and 4.20, the algorithm fails to assign a thickness to points on the object surface. This is due to the roughness of the surface and the slightly tilted surface planes. In both cases, the center of the sphere is shifted outside of the image and is automatically discarded. This is justified, as for most cases the calculated thickness of these points would be incorrect.

Nevertheless, even with 65% of omitted points, the mean thickness is still based on 3'500 individual thickness measurements.

These results indicate that accuracy is directly linked with the voxel size, as a higher resolution leads to a higher accuracy and vice versa.

A total of three measurements might not be enough to obtain a very reliable accuracy and precision measurement, however it does provide an estimate of the measurement range. These values, are used to define the lower limits for the final 3D model.

Chapter 5

Sample Scans

5.1 Introduction

For the ”real” sample scans, young healthy Wistar rats [21] were used. The rat legs were dissected from the body at the hip joint and the skin and fat layers were removed (see figure 5.1).

Figure 5.1: Dissected Wistar rat leg.

To prevent the sample from drying out, and to avoid air/water interface artifacts, the sample was wrapped in an elastic paraffin foil (Parafilm).

For multi-modality registration purposes, four fiducial markers were placed around the knee joint. The fabrication and attachment procedures are described into more detail in subchapter 7.2.1. The sample was than placed inside a plastic tube and fixed with Styrofoam to prevent movement during or between the scans (see figure 5.2).

Figure 5.2: Rat knee in plastic tube, immobilized with Styrofoam.

5.2 Scan Methods

Different scan methods have been tried out, to obtain images with good tissue contrast and high signal to noise ratio. The following subchapters describe each acquisition protocol used.

5.2.1 MRI without Contrast Agent

The sample preparation was performed one hour prior to the first scan. For both MRI and CT scans, the same scan protocol was used as in the phantom experiments described in Chapter 4.

MRI scans were taken first, as it is more time intensive and availability is scarce. The sample was carefully placed inside a 35mm quadrature (two channel) receiver coil. The coil is matched and tuned at a frequency of 400.5 MHz to obtain a 50Ω impedance.

With the sample placed in the 9.4T bore MRI device, the Bruker MRI software runs an automatic shim, to optimize the output signal of the coil. This step is followed by manual shimming to eliminate any existing inhomogeneities. Finally the parameters from the scan protocol (see table B.2) are set and the scan initiated.

5.2.2 MRI Scan with Contrast Agent

In principle, all the processing steps remained the same as for the MRI scan without contrast agent. The difference is that the sample was soaked for 24, 36 or 48 hours in a 5% (vol/vol) Magnevist [3] solution, manufactured by Berlex, USA, before it was wrapped in Parafilm. The contrast agent is supposed to enhance contrast between different soft-tissue types and simultaneously decrease the intensity of the tissue

surface, to more easily distinguish between organs with similar magnetic resonance properties.

5.2.3 CT Scan without Contrast Agent

Immediately after the MRI scan was completed, the sample was carefully transported to the CT lab, with efforts made not to induce any change in position of the rat knee joint. The scan area was set, such that the knee joint and all four fiducial markers were within the scan range. All remaining parameters were set according to table B.1.

5.2.4 CT Scan with Contrast Agent

Unlike MRI, the contrast between different tissue types cannot be altered for CT scans, as the data acquisition is based on fixed attenuation properties of the tissue. Therefore, the X-ray based imaging methods are mostly focused on visualizing bone structures. Nevertheless, the visibility of soft-tissue can be enhanced with the help of contrast agent.

Since the phantom experiments showed that accuracy and precision for structures smaller than 600μm decrease rapidly for MRI, it would be advantageous to extract the rat knee cartilage, with an average thickness of 400μm, using the CT image.

Different CT-contrast agents have been tested:

- **Optiray from Mallinckrodt Inc. [25]:** Is a standard iodine contrast agent frequently used for clinical CT scans.
- **$BaSO_4$ from EZEM Canada [9]:** Is an MRI compatible CT contrast agent mainly used in the field of gastroenterology.
- **Fenestra LC from Alerion Biomedical Inc. [2]:** Is a novel contrast agent used only in animal studies. The agents are primarily developed for oncology and vascular research.

Basically two methods to apply the contrast agent were considered:

- **Injection:** 0.1 to 0.3ml of pure contrast agent was directly injected into the synovial capsule. After various test injections, a frontal injection through the ligament of the patella, seamed to work best.
- **Soaked:** The samples were immersed in a contrast agent bath with different concentrations (10-100%) for different durations (1-24 hours). Only Optiray and Fenestra LC have been used for these experiments.

5.3 Results

The results of only one scan per acquisition method are presented here. The findings are extensively discussed in the following chapter.

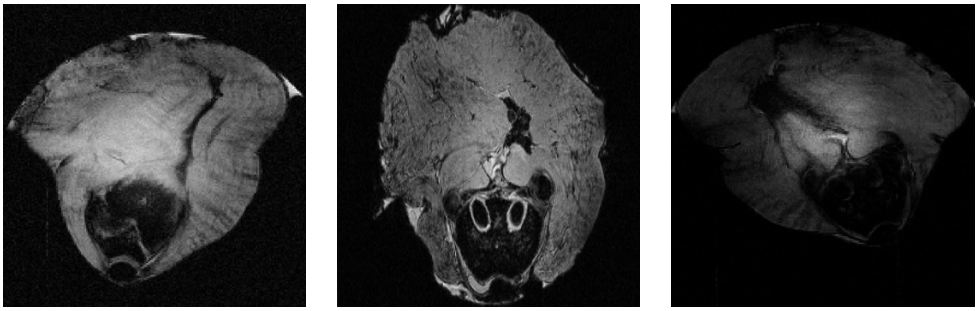

Figure 5.3: MR image slices after the sample was soaked in Magnevist for 24 hours (left), 36 hours (center) respectively 48 hours (right).

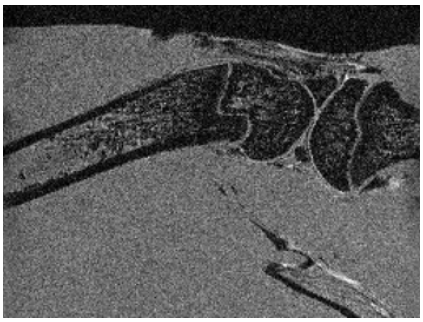

Figure 5.4: Image slice of MRI scan without contrast agent.

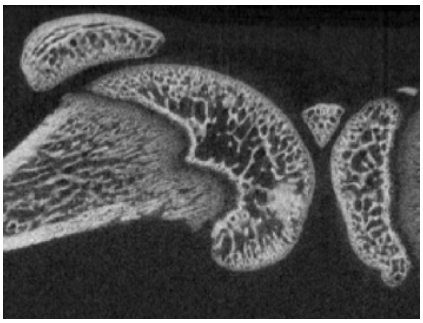

Figure 5.5: Image slice of CT scan without contrast agent.

Figure 5.6: Inhomogeneous distribution of injected contrast agent (Fenestra LC) in the synovial capsule of a rat knee joint.

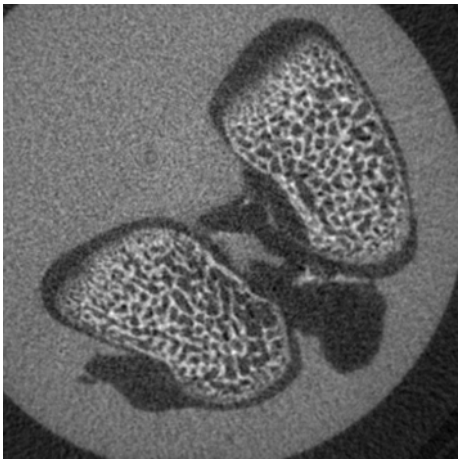

Figure 5.7: Image slice of contrast enhanced CT scan (Fenestra LC, immersed).

5.4 Discussion

3D gradient-echo MRI scans without contrast agent return high intensities for soft-tissue. Although good contrast between different soft-tissue types is achieved, the edges intensities between tissues of the same type are poor, as shown in figure 5.4.

Significantly better results are achieved if the samples are soaked first in contrast agent. Therefore, the concentration and the immersion time have a significant influence on the image quality.

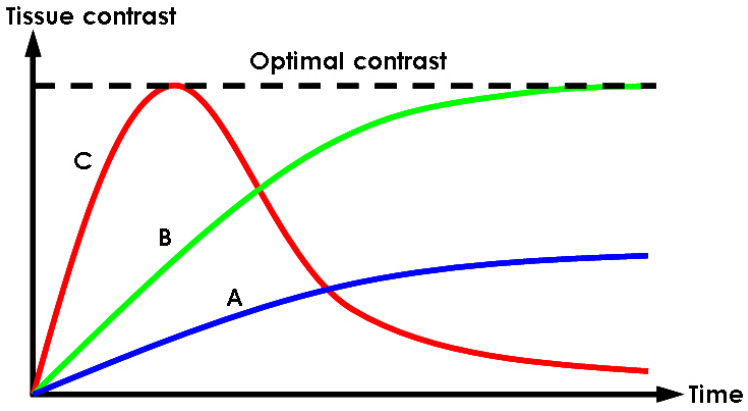

Figure 5.8: Tissue contrast for soaked samples over time with a too low (A), optimal (B) and too high (C) contrast agent concentration.

Figure 5.8 illustrates the relationship between the immersion time and the tissue contrast. If the concentration is optimal, the maximal contrast C_{max} is reached after a certain time t_{Opt} and remains stable on this level (curve B). Otherwise, if the level of contrast agent is too low, the optimal contrast level is never reached (curve A). On the other hand, if the contrast agent level is too high, the maximum contrast level is reach rapidly, but decreases again, due to contrast agent saturation of the tissue (curve C).

The optimal concentration estimate of 5% (vol/vol) Magnevist solution was based on the expertise of the MRI personal. Preliminary tests indicated that this concentration was slightly too high as the results from an immersion time of 24 and 48 hours returned slightly worse soft-tissue contrasts, then 36 hours did (see figures 5.3). Thus, the sample used for the 3D knee joint model, was soaked for 36 hours.

For future studies it would be recommended that the optimal concentration or a concentration slightly below optimal is found and used. If the concentration of

the contrast is too high, it might not have diffused through to the center, while the outermost tissue regions already have surpassed the optimal concentration.

Due to a slightly eccentric positioning of the sample in the static magnetic field, an intensity drift in the lower half of the image occurred (figure 5.3, middle). The static magnetic field is only constant in an area of 10cm^2 and decreases rapidly toward each end. A change in the static magnet field strength results in a change in the Larmor spin frequency and leads to the observed signal loss.

The CT scans without contrast agent returned excellent, artifact and distortion free, high resolution images of the bone structure. Due to the high resolution, and the relatively big volume of interest, the AIM files were large with sizes ranging 70 and 140MB. This may lead to problems in the subsequent registration and segmentation processing steps.

Both methods (i.e. contrast injection and immersion) for contrast-enhanced CT scans failed to return useful results.

Using CT contrast injection, the synovial capsule target-site was often missed or, if the injection was successful, the contrast agent did not disperse homogeneously (see figures 5.6).

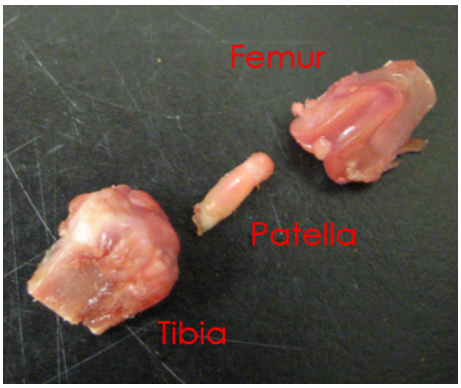

Figure 5.9: Dissected femur and tibia growth plates and the patella.

For the samples immersed in Optiray, even experimenting with time and concentration variations did not return any satisfactory results. Optiray brightened soft-tissue, however it was still orders of magnitude from the MR image quality apart. Furthermore, cartilage, the main reason for the use of CT contrast agent, was still not visible.

Fenestra and $BaSO_4$ are non-diffusive contrast agents. Therefore, the knee sample had to be dissected down to the two, individual knee joint growth plates covered by cartilage. Figure 5.9 shows the dissected femur and tibia growth plates just prior to being soaked in a Fenestra bath and then scanned immediately.

Due to Fenetra's and $BaSO_4$'s non-diffusive properties, the edges between cartilage and bone, were clearly visible (illustrated in figure 5.7). Great care should be taken while freeing the sample from the soft-tissue. To maintain the condition of the cartilage it must not be damaged or scratched by the scalpel. However, it is important to remove all the surrounding soft-tissue to ease the subsequent cartilage segmentation.

A major drawback of this method is the destructive nature of the dissection, which is obviously not applicable for potential future in-vivo experiments.